

# Laterally Driven Polysilicon Resonant Microstructures

William C. Tang, Tu-Cuong H. Nguyen, and Roger T. Howe

University of California at Berkeley  
Department of Electrical Engineering and Computer Sciences  
and the Electronics Research Laboratory  
Berkeley Sensor & Actuator Center  
Berkeley, California 94720

## Abstract

Interdigitated finger (comb) structures are demonstrated to be effective for electrostatically exciting the resonance of polysilicon microstructures parallel to the plane of the substrate. Linear plates suspended by a folded-cantilever truss and torsional plates suspended by spiral and serpentine springs are fabricated from a 2  $\mu\text{m}$ -thick phosphorus-doped LPCVD polysilicon film. Resonance is observed visually, with frequencies ranging from 18 kHz to 80 kHz and quality factors from 20 to 130. Simple beam theory is adequate for calculating the resonant frequencies, using a Young's modulus of 140 GPa and neglecting residual strain in the released structures.

## I. INTRODUCTION

Resonant micromechanical structures are used as transducing elements in a wide variety of sensors. These devices utilize the high sensitivity of the frequency of a mechanical resonator to physical or chemical parameters which affect its potential or kinetic vibrational energy [1-4]. Microfabricated resonant structures for sensing pressure [5-7], acceleration [8], and vapor concentration [9] have been demonstrated.

Mechanical vibration of microstructures can be excited in several ways, including piezoelectric films [5], thermal expansion [8,10], electrostatic forces [1,6], and magnetostatic forces [7]. Vibration can be detected by means of piezoelectric films [5], piezoresistive strain gauges [10], optical techniques [10,11], and capacitively [1,6,9]. Electrostatic excitation combined with capacitive (electrostatic) detection is an attractive approach for silicon microstructures because of simplicity and compatibility with micromachining technology [1,2].

Both crystalline silicon [6] and polycrystalline silicon (polysilicon) [9] microstructures have been driven and sensed electrostatically by means of fixed electrodes forming parallel-plate capacitors with the structure. However, there are several drawbacks to the parallel-plate-capacitor drive and sense of micromechanical structures. The electrostatic force is nonlinear unless the amplitude of vibration is limited to a small fraction of the capacitor gap. In addition, the quality factor  $Q$  of the resonance is very low at atmospheric pressure because of squeeze-film damping in the micron-sized capacitor gap [9]. If the microstructure is resonated in vacuum, the efficient parallel-plate excitation and the very high intrinsic  $Q$  lead to steady-state excitation voltages with mV-level amplitudes. Such low voltage levels complicate the design of the sustaining amplifier [12].

In this paper, we describe the design, fabrication, and initial testing of an electrostatic comb structure for exciting and sensing the vibration of polysilicon microstructures *parallel* to the plane of the substrate. Interdigitated fingers and the mechanical structure are etched in a single LPCVD polysilicon film, which has

been deposited on a patterned sacrificial oxide layer. The drive capacitance is linear with displacement of the structure, resulting in a force which is independent of the vibration amplitude. Moreover, the vibration amplitude can be of the order of 10  $\mu\text{m}$  for certain comb and structure designs. The use of weaker fringing fields to excite resonance is advantageous for high- $Q$  structures (resonating in vacuum), since this results in larger steady-state excitation voltages. Furthermore, the quality factor for lateral vibration at atmospheric pressure is substantially higher than for vibration normal to the substrate [13,14]. Couette flow in the gap between the structure and the substrate occurs for lateral motion of the structure, which is much less dissipative than squeeze-film damping [13]. Another significant advantage of the lateral-drive concept is that a variety of elaborate geometric structures, such as differential capacitive excitation and detection, can be incorporated without an increase in process complexity. This flexibility is being exploited in current efforts to develop a microactuator technology based on lateral resonant structures [15].

The theory of the electrostatic comb drive is derived first and used to obtain electromechanical transfer functions for generalized lateral structures. We next present the design and modeling of a linear resonant structure with a truss suspension and a torsional resonant structure using a spiral-spring suspension or a serpentine-spring suspension. The fabrication process, a straightforward application of surface micromachining technology, is then described. Initial measurements of resonant frequencies and quality factors are compared with analytical and finite-element calculations.

## II. ELECTROSTATIC COMB DRIVE

Figure 1 shows the layout of a linear resonant structure which can be driven electrostatically from one side and sensed capacitively at the other side with interdigitated finger (comb) structures. Alternatively, the structure can be driven differentially (push-pull) using the two combs, with the motion sensed by the impedance shift at resonance [12]. In analyzing the electromechanical transfer function, we consider the former, two-port configuration. The motion is sensed by detecting the short-circuit current through the time-varying interdigitated capacitor with a  $dc$  bias [1].

The driving force and the output sensitivity are both proportional to the variation of the comb capacitance  $C$  with the lateral displacement  $x$  of the structure. A key feature of the electrostatic-comb drive is that  $(\partial C / \partial x)$  is a constant, independent of the displacement  $x$ , so long as  $x$  is less than the finger overlap (Fig. 1). Therefore, electrostatic-comb drives can have linear electromechanical transfer functions for large displacements, in contrast to parallel-plate capacitive drives.

At the sense port, harmonic motion of the structure in Fig. 1 results in a sense current  $i_s$  which is given by

$$i_s = V_S (\partial C / \partial x) (\partial x / \partial t), \quad (1)$$

where  $V_S$  is the bias voltage between the structure and the stationary sense electrode. At the drive port, the static displacement  $x$  as a function of drive voltage is given by

$$x = \frac{F_x}{k_{sys}} = \frac{1/2 v_D^2 (\partial C / \partial x)}{k_{sys}}, \quad (2)$$

where  $F_x$  is the electrostatic force in the  $x$ -direction,  $k_{sys}$  is the system spring constant, and  $v_D$  is the drive voltage.

For a drive voltage  $v_D(t) = V_p + v_d \sin(\omega t)$ , the time derivative of  $x$  is

$$\begin{aligned} \frac{\partial x}{\partial t} &= \frac{(\partial C / \partial x)}{2k_{sys}} \frac{\partial (v_D^2)}{\partial t} \\ &= \frac{(\partial C / \partial x)}{2k_{sys}} \left[ 2\omega V_p v_d \cos(\omega t) + \omega v_d^2 \sin(2\omega t) \right], \end{aligned} \quad (3)$$

where we have used the fact that  $(\partial C / \partial x)$  is a constant for the interdigitated-finger capacitor. The second-harmonic term on the right-hand-side of Eqn. (3) is negligible if  $v_d \ll V_p$ . Furthermore, if a push-pull drive is used, this term results in a common-mode force and is cancelled to first order. At mechanical resonance, the magnitude of the linear term in Eqn. (3) is multiplied by the

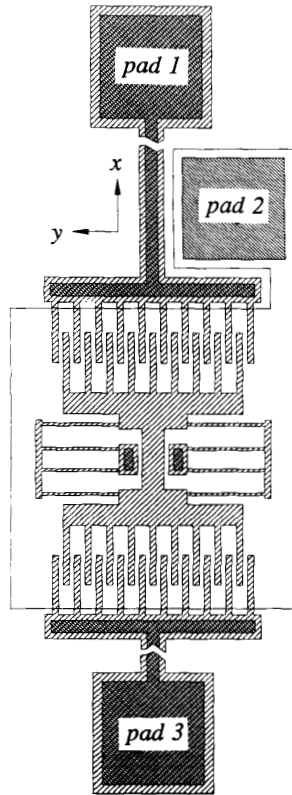


Fig. 1. Layout of a linear resonant plate with comb structures on both ends and a 50  $\mu\text{m}$ -long folded-beam on each side.

quality factor  $Q$  [1,9], from which it follows that the magnitude of the transfer function  $T(j\omega_r) = X / V_d$  relating the phasor displacement  $X$  to phasor drive voltage  $V_d$  at the resonant frequency  $\omega_r$  is:

$$\left| \frac{X}{V_d} \right| = V_p \frac{Q}{k_{sys}} (\partial C / \partial x). \quad (4)$$

The transconductance of the resonant structure is defined by  $G(j\omega) = I_s / V_d$ . Its magnitude at resonance can be found by substitution of Eqn. (4) into the phasor form of Eqn. (1):

$$\left| \frac{I_s}{V_d} \right| = \omega V_p V_S \frac{Q}{k_{sys}} (\partial C / \partial x)^2. \quad (5)$$

A planar electrode extends under the the comb and plate in Fig. 1, which can be grounded or set to a  $dc$  potential in order to minimize parasitic capacitive coupling between the drive and sense ports. An additional function of this electrode is to suppress the excitation of undesired modes of the structure.

### III. RESONANT STRUCTURE DESIGN

We now consider the mechanical design of two classes of lateral resonant structures which demonstrate the power and flexibility of the lateral drive approach: linear resonant plates with folded supporting beams and torsional resonant plates with differential drive and sense ports.

#### A. Linear Resonant Plates

Figure 1 shows the layout of a linear resonant plate with a 50  $\mu\text{m}$ -long folded-beam suspension. Motivations for this truss suspension are its large compliance and its capability for relief of built-in residual strain in the structural film. The folded cantilever beams are anchored near the center, thus allowing expansion or contraction of the four beams along the  $y$ -axis (Fig. 1). Both the average residual stress in the polysilicon film and stress induced by large-amplitude plate motion should be largely relieved by this design. In addition, the long effective support lengths result in a highly compliant suspension. Plates with 200  $\mu\text{m}$ -long trusses are resonated with amplitudes as large as 10  $\mu\text{m}$ .

An accurate analytical expression for the fundamental lateral resonant frequency,  $f_r$ , can be found using Rayleigh's Method:

$$f_r = \frac{1}{2\pi} \left[ \frac{k_{sys}}{(M_p + 0.3714M)} \right]^{\frac{1}{2}}, \quad (6)$$

where  $M_p$  and  $M$  are the masses of the plate and of the supporting beams, respectively. For the folded-beam structure, an analytical expression  $k_{sys}$  can be found by assuming that the trusses joining the folded beam segments are rigid:

$$k_{sys} = 24EI/L^3 = 2Eh(W/L)^3. \quad (7)$$

where  $I = (1/12)hW^3$  is the moment of inertia of the beams. Residual strain in the structure is neglected in finding this expression. Combining Eqs. (6) and (7), it follows that

$$f_r = \frac{1}{2\pi} \left[ \frac{2Eh(W/L)^3}{(M_p + 0.3714M)} \right]^{\frac{1}{2}}. \quad (8)$$

The quality factor  $Q$  is estimated by assuming that Couette flow underneath the plate is the dominant dissipative process [14]:

$$Q = \frac{d}{\mu A_p} (Mk_{sys})^{\frac{1}{2}}, \quad (9)$$

where  $\mu$  is the absolute viscosity of air ( $1.8 \times 10^{-5} \text{ N} \cdot \text{s} \cdot \text{m}^{-2}$ ), and  $d$  is the offset between the plate and the substrate. Quality factors for lateral motion are much higher than for motion normal to the substrate [9,16].

### B. Torsional Resonant Plates

Another class of structures is driven into torsional resonance by a set of concentric interdigitated electrodes. Figure 2 shows one of the designs with two Archimedean spirals as supporting beams. Figure 3 is a scanning-electron micrograph (SEM) of of

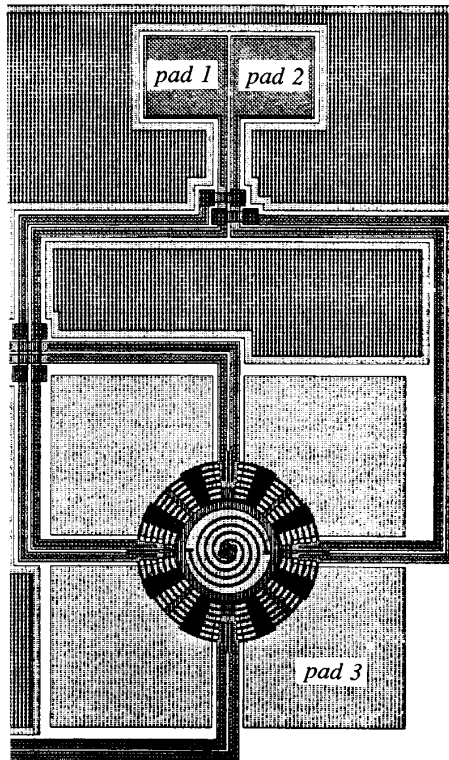


Fig. 2. Layout of a torsional resonant plate with 4 pairs of balanced concentric comb structures supported by two spirals.

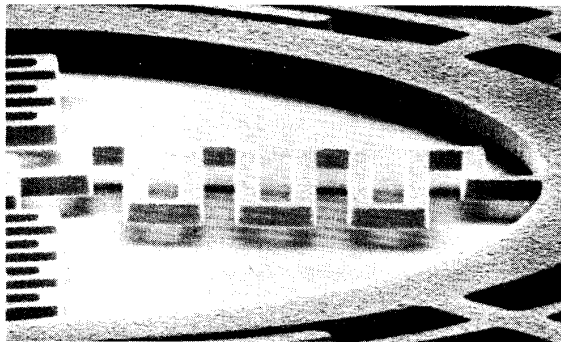


Fig. 3. SEM micrograph of a serpentine spring supporting a torsional resonant plate.

another design using four serpentine springs. The structures are supported only at the center, enabling some relaxation of the built-in residual stress in the polysilicon film. An advantage of the torsional approach is that four or more pairs of balanced concentric comb structures can be placed at the perimeter of the ring, allowing a high degree of flexibility for differential drive and sense. Since both the drive and the sense ports are differentially balanced, excitation of undesired oscillation modes is avoided and signal corruption by feedthrough is minimized. As with the lateral structure, extensive ground planes are utilized.

The torsional spring constant of the Archimedean spiral is given by [17]:

$$k_{\theta} = \frac{EhW^3}{12L} \quad (\mu\text{N} \cdot \mu\text{m} \cdot \text{rad}^{-1}), \quad (10)$$

where  $L$  is the length of the spiral. As was done for the lateral resonant structures, residual strain in the spiral spring is neglected in the analysis. This assumption will be reexamined in the discussion of the measured resonant frequencies.

The torsional resonant frequency,  $f_{\theta}$ , is evaluated by replacing  $k_{\text{sys}}$  in Eq. (6) with the torsional spring constant,  $k_{\theta}$ , and the masses,  $M_p$  and  $M$ , with the mass moments of inertia,  $J_p$  and  $J$ :

$$f_{\theta} = \frac{1}{2\pi} \left[ \frac{k_{\theta}}{J_p + 0.3714J} \right]^{\frac{1}{2}}. \quad (11)$$

The value of  $J$  can be found by evaluating the following integral over an appropriate limit:

$$J = \int r^2 dM = \rho h \iint r^3 d\theta dr, \quad (12)$$

where  $\rho$  is the density of polysilicon ( $2.3 \times 10^3 \text{ kg} \cdot \text{m}^{-3}$ ).

The quality factor is estimated similarly to Eq. (9) by assuming Couette flow underneath the plate, and is given by

$$Q = \frac{d(Jk_{\theta})^{\frac{1}{2}}}{\mu \int r^2 dA_p} \quad (13)$$

## IV. FABRICATION PROCESS

The structures are fabricated with the four-mask process illustrated in Fig. 4. A significant advantage of this technology is that all the critical features are defined with one mask, eliminating errors due to mask-to-mask misalignment. The process begins with a standard  $\text{POCl}_3$  blanket n+ diffusion, which defines the substrate ground plane, after which the wafer is passivated with a layer of 1500 Å-thick low-pressure chemical-vapor-deposited (LPCVD) nitride deposited on top of a layer of 5000 Å-thick thermal  $\text{SiO}_2$  (Fig. 4(a)). Contact windows to the substrate ground plane are then opened (Fig. 4(b)) using a combination of plasma and wet etching.

The next steps involve deposition and definition of the first polysilicon layer. A layer of 3000 Å-thick, *in situ* phosphorus-doped polysilicon is deposited by LPCVD at 650°C then patterned with the second mask (Fig. 4(c) and 4(d)). This layer serves as a second electrode plane, the interconnection to the n+ diffusion, and for standoff bumps to prevent sticking of the second polysilicon layer to the substrate after the final micromachining step. (Standoff bumps are not included in the initial process run.) A 2 μm-thick LPCVD sacrificial phosphosilicate glass (PSG) layer is deposited and patterned with the third mask, as shown in Figs. 4(e) and 4(f), which defines the anchors of the microstructures.

The 2  $\mu\text{m}$ -thick polysilicon structural layer is then deposited by LPCVD (undoped) at 605°C (Fig. 4(g)). The structural layer is doped by depositing another layer of 3000 Å-thick PSG (Fig. 4(h)) and then annealing at 950°C for one hour. This doping process is designed to dope the polysilicon symmetrically by diffusion from the top and the bottom layers of PSG. A stress-annealing step is then optionally performed at 1050°C for 30 minutes in  $\text{N}_2$ . The annealing temperature is lower than 1100°C in order to avoid loss of adhesion between the PSG and the  $\text{Si}_3\text{N}_4$  [12,16].

After stripping the top PSG layer by a timed etch in 10:1 HF, the plates, beams, and electrostatic comb drive and sense structures are defined in the final masking step (Fig. 4(i)). The structures are anisotropically patterned in a  $\text{CCl}_4$  plasma by reactive-ion etching, in order to achieve nearly vertical sidewalls. Figure 4(j) illustrates the final cross section after the wafer is immersed in 10:1 diluted HF to etch the sacrificial PSG. The

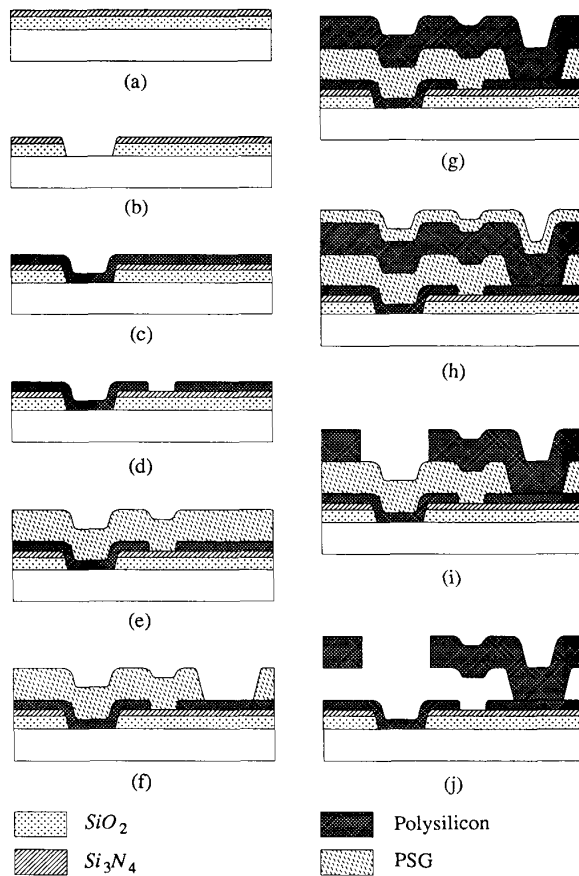


Fig. 4. Process sequence of a lateral resonant structure. (a) Deposition of LPCVD nitride on top of a layer of thermal  $\text{SiO}_2$ . (b) Contact windows to substrate  $n^+$  diffusion. (c) Deposition of *in situ* P-doped LPCVD polysilicon. (d) Patterning of first polysilicon layer. (e) Deposition of sacrificial PSG. (f) Anchor windows for second polysilicon layer. (g) Deposition of the undoped LPCVD polysilicon structural layer. (h) Deposition of second layer of PSG for doping symmetry. (i) Patterning of second polysilicon layer. (j) Final cross section after wet etching of sacrificial PSG.

wafer is rinsed repeatedly with DI water for at least 30 minutes after the micromachining step is completed and then dried in a standard spin dryer.

Surface-micromachined polysilicon structures can become stuck to the substrate after the final drying process [18]. The yield of free-standing structures is zero on wafers for which the 30-minute stress anneal at 1050°C is omitted. When the stress anneal is included in the process, 70% of the structures are free-standing. The 30% which are initially attached to the substrate could be freed easily with a probe tip; the high flexibility of the structures allows manipulation without breakage. No amount of probing, however, could free any of the unannealed structures.

A series of clamped-clamped microbridges is used to estimate the average residual strain in the structural polysilicon film from the minimum buckling length [19]. The moment of the residual strain is qualitatively studied by a series of clamped-free cantilever beams. Since the microbridges have "step-up" anchors, it is expected that end effects will have to be modeled carefully to obtain an accurate value of the residual strain [20]. Moreover, the "stiction" of the diagnostic microbridges and cantilevers to the substrate during drying is also a source of error in calculating the strain and its moment [21].

For the unannealed samples, the microcantilevers have a tendency to deflect and attach to the substrate for lengths greater than 150  $\mu\text{m}$ . We interpret the buckling length of about 120  $\mu\text{m}$  for microbridges using the simple clamped-clamped Euler's criterion [19] and estimate the strain as about  $10^{-3}$ . Annealed samples have apparently undeflected cantilevers under optical and SEM observation and have a buckling length of about 220  $\mu\text{m}$ , indicating a residual strain of about  $3 \times 10^{-4}$ . These estimated values are typical of residual strain for phosphorus-doped polysilicon.

Figures 5–8 are scanning-electron micrographs of the completed structures.

## V. EXPERIMENTAL MEASUREMENTS

The resonant frequencies, quality factors, and transfer function of the structures with beam lengths of 80  $\mu\text{m}$  or longer can be found by visual observation under 25X magnification. Sinusoidal and *dc* bias voltages are applied to the structures via probes contacting the numbered polysilicon pads in Figs. 1 and 2. For the linear structures, the sinusoidal drive voltage is applied to one set of fixed electrode fingers via *pad 3*, while a *dc* bias is supplied to *pad 1* (connected to the dormant sense fingers) and *pad 2* (connected to the first-level polysilicon ground plane and to the suspended structure). The diffused ground plane is left floating in the initial measurements. The dormant fingers are biased to eliminate electrostatic attraction between them and the resonant structure. For the torsional structures (Fig. 2), the sinusoidal voltage is applied to the drive fingers via *pad 2*, and the dormant sense fingers, ground plane, and resonant structure are biased via *pad 1* and *pad 3*.

In order to provide large-amplitude lateral motion in air for visual observation, *dc* biases of up to 40 V and driving voltage amplitudes (zero to peak) of up to 10 V are used. Resonant frequencies are determined by maximizing the amplitude of vibration, which can be as large as 10  $\mu\text{m}$  for the linear structures with the longest support beams. The measured resonant frequencies for the linear structures are listed in Table I and those for the torsional structures are listed in Table II. The results include measurements from two different electrostatic comb designs (type A and type B), which are described in the figure with Table I.

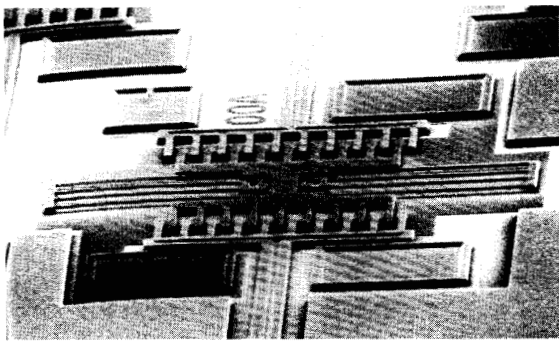


Fig. 5. SEM micrograph of a linear resonant structure with 100  $\mu\text{m}$ -long beams.

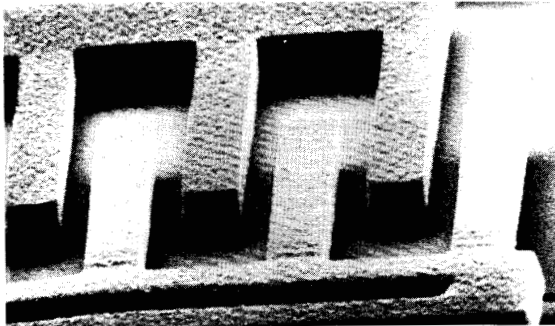


Fig. 6. SEM micrograph of the linear comb structure.

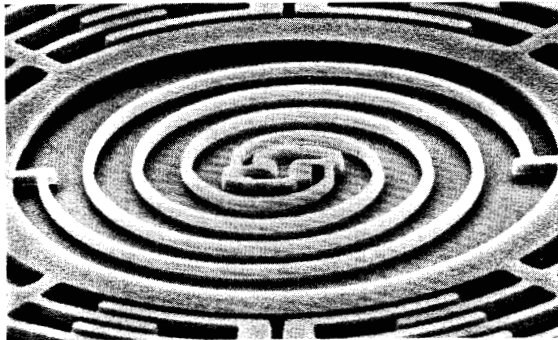


Fig. 7. SEM micrograph of two two-turn Archimedean spirals supporting a torsional resonant plate.

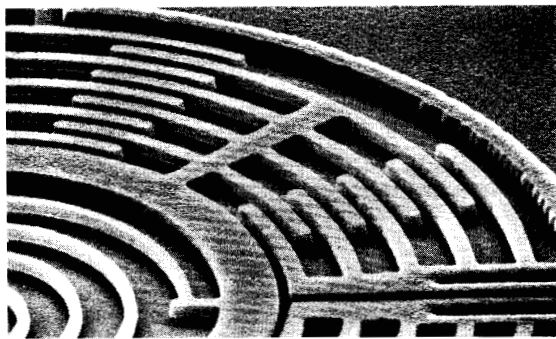
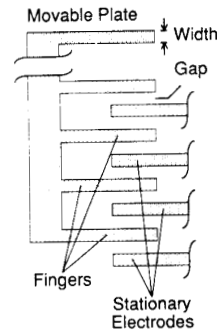


Fig. 8. SEM micrograph of the concentric comb structure.

TABLE I  
Predicted and Measured Resonant Frequency Values  
of the Linear Resonant Structures

| Beam length<br>[ $\mu\text{m}$ ] | Type A             |                   | Type B             |                   |
|----------------------------------|--------------------|-------------------|--------------------|-------------------|
|                                  | Predicted<br>[kHz] | Measured<br>[kHz] | Predicted<br>[kHz] | Measured<br>[kHz] |
| 80                               | 75.5               | $75.0 \pm 0.05$   | 71.8               | $72.3 \pm 0.05$   |
| 100                              | 53.7               | $54.3 \pm 0.05$   | 51.1               | $50.8 \pm 0.05$   |
| 120                              | 40.6               | $41.1 \pm 0.1$    | 38.7               | $39.4 \pm 0.1$    |
| 140                              | 32.0               | $32.0 \pm 0.2$    | 30.5               | $30.0 \pm 0.2$    |
| 160                              | 26.0               | $25.9 \pm 0.2$    | 24.8               | $25.0 \pm 0.2$    |
| 180                              | 21.7               | $21.5 \pm 0.3$    | 20.7               | $20.3 \pm 0.3$    |
| 200                              | 18.4               | $18.2 \pm 0.3$    | 17.6               | $17.5 \pm 0.3$    |



Types A and B Features

| Features   | A  | B   |
|--|----|-----|
| # of fingers   | 9  | 11  |
| Width [ $\mu\text{m}$ ]  | 4  | 4   |
| Gap [ $\mu\text{m}$ ]  | 3  | 2   |
| Fitted $\partial C / \partial x$ [ $\text{aF}\mu\text{m}^{-1}$ ] | 58 | 150 |

TABLE II  
Predicted and Measured  
Resonant Frequency Values  
of the Torsional Resonant Structures

| Supporting<br>Beam Type | Predicted<br>[kHz] | Measured<br>[kHz] |
|-------------------------|--------------------|-------------------|
| Spiral                  | 10.5               | $9.7 \pm 0.3$     |
| Serpent                 | 60.7               | $59.4 \pm 0.2$    |

The calculated resonant frequencies in Tables I and II are found from Eqns. (8) and (9) with the Young's modulus adjusted to give the best fit to the experimental data. For the serpentine-spring torsional structures, a finite-element program [22] is used to find the effective spring constant. The best-fit value for Young's modulus is  $E = 140$  GPa for both linear and torsional resonant structures. From Table I and II, the calculated and measured resonant frequencies are in close agreement for all the lateral structures.

Initial visual measurements of the quality factor  $Q$  are plotted in Fig. 9 for the linear resonant structures. The visual measurement of  $Q$  is especially difficult for structures with small vibration amplitudes, which is reflected in the larger error bars for these points. The calculated quality factors from Eqn. (9) are consistently higher than the measured values, indicating that the assumption of pure Couette flow is an oversimplification for these structures. However, the calculated values of  $Q$  are of the correct magnitude and may be useful for design. The highest measured  $Q$  is about 130 for a structure with 80  $\mu\text{m}$ -long folded-beam suspension.

The magnitude of the electromechanical transfer function is measured by estimating the amplitude of vibration from the envelope of the blurred vibrating structure at a given drive voltage and bias voltage. Figure 10 is a comparison of the experimental results for the linear resonant structures with the calculated values from Eqn. (4), for which the capacitance variation ( $\partial C / \partial x$ ) for the two types of comb drives is a fitting parameter. The type A drive is found to have  $\partial C / \partial x = 58 \text{ aF}\mu\text{m}^{-1}$  and the type B has  $\partial C / \partial x = 150 \text{ aF}\mu\text{m}^{-1}$ . These experimental results are about a factor of five less than the variation found by a simple two-dimensional simulation using a Green's function approach. However, the proximity of the comb to the substrate was neglected in the simulation.

Electrical characterization of the structures is being pursued. Since there is no integrated buffer circuit, the sense current tends to be swamped by feedthrough [12,16]. The differential drive and sense torsional two-port resonant structure is attractive for minimizing feedthrough.

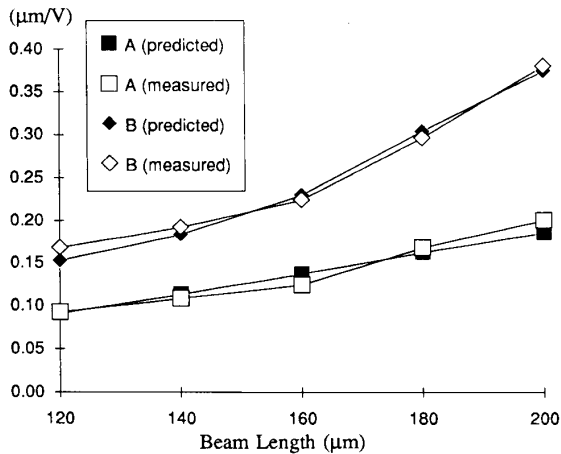


Fig. 10. Predicted and measured magnitude of the electromechanical transfer function for the linear resonant structures. The values are obtained at  $V_p = 40\text{V}$ . The fitting parameter,  $\partial C / \partial x$ , is found to be  $58 \text{ aF}\mu\text{m}^{-1}$  for type A comb drive and  $150 \text{ aF}\mu\text{m}^{-1}$  for type B.

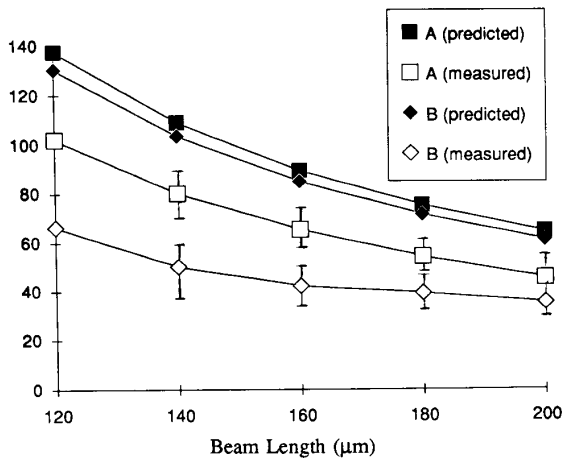


Fig. 9. Predicted and measured  $Q$  for types A and B linear resonant structures with different beam length.

## VI. CONCLUSIONS

This paper has demonstrated the feasibility and outlined some of the design issues for the electrostatic comb drive and detection of laterally resonant polysilicon microstructures. From the initial visual measurements, it appears that the first-order theory for the transfer function and resonant frequency are adequate for predicting the observed behavior. However, the quality factor calculated from Couette drag due to shear flow beneath the structure consistently overestimates  $Q$ . It is likely that dissipation due to the air movement in the interdigitated fingers is a significant cause of the lower measured quality factors.

The measured resonant frequencies are accurately predicted for all the linear and torsional structures by simple beam theory, using a Young's modulus of 140 GPa and neglecting the residual strain in the released structures. The excellent fit with the measured frequencies over a range of truss dimensions and for the spiral and serpentine springs suggests that the residual strain is effectively relieved in these structures. Otherwise, it would be expected that a shift in frequency from the simple unstrained theory would be observed, with a greater shift for the shorter beams [11]. The value of 140 GPa is less than that measured for fine-grained, undoped polysilicon [11] and greater than that measured for phosphorus-doped, rapid-thermal-annealed polysilicon [23].

An important topic for further research is the simulation and verification of the resonant modes for these complex microstructures [24]. At atmospheric pressure, those modes with motion normal to the substrate are heavily damped, which greatly relaxes the design constraints on the electrostatic comb. For operation in vacuum, design of the drive structure to ensure excitation of a single mode will be challenging, due to the high intrinsic  $Q$  of polysilicon microstructures.

### Acknowledgements

The authors wish to thank Y.-C. Tai for help with process development, L.-S. Fan for advice on polysilicon properties and for the Green's function solver, S. Hoagland, and R. M. Hamilton, and K. Voros of the UC Berkeley Microfabrication Facility for invaluable assistance in processing the devices.

### REFERENCES

- [1] R. T. Howe, "Resonant microsensors," *Technical Digest*, 4<sup>th</sup> International Conference on Solid-State Sensors and Actuators, Tokyo, Japan, June 2-5, 1987, 843-848.
- [2] M. A. Schmidt and R. T. Howe, "Resonant structures for integrated sensors," *Technical Digest*, IEEE Solid-State Sensor Workshop, Hilton Head Island, South Carolina, June 2-5, 1986.
- [3] R. M. Langdon, "Resonator sensors - a review," *J. Phys. E., Sci. Inst.*, **18**, 103-115, (1985).
- [4] E. P. EerNisse and J. M. Paros, "Practical considerations for miniature quartz resonator force transducers," *Proceedings*, 28<sup>th</sup> ISA International Instrumentation Symposium, 1982, 33-44.
- [5] J. G. Smits, H. A. C. Tilmans, and T. S. J. Lammerink, "Pressure dependence of resonant diaphragm pressure sensors," *Technical Digest*, 3<sup>rd</sup> International Conference on Solid-State Sensors and Actuators, Philadelphia, Pennsylvania, June 11-14, 1985, 93-96.

- [6] J. C. Greenwood, "Etched silicon vibrating sensor," *J. Phys. E., Sci. Inst.*, **17**, 650-652, (1984).
- [7] K. Ikeda, *et al*, "Silicon pressure sensor with resonant strain gauges built into diaphragm," *Technical Digest*, 7<sup>th</sup> Sensor Symposium, Tokyo, Japan, May 30-31, 1988, 55-58.
- [8] D. C. Satchell and J. C. Greenwood, "Silicon microengineering for accelerometers," *Proc. Inst. of Mech. Eng.*, **1987-2**, Mechanical Technology of Inertial Devices, Newcastle, England, April 7-9, 1987, 191-193.
- [9] R. T. Howe and R. S. Muller, "Resonant-microbridge vapor sensor," *IEEE Trans. on Electron Devices*, **ED-33**, 499-506, (1986).
- [10] W. Benecke, *et al*, "Optically excited mechanical vibrations in micromachined silicon cantilever structures," *Technical Digest*, 4<sup>th</sup> International Conference on Solid-State Sensors and Actuators, Tokyo, Japan, June 2-5, 1987, 838-842.
- [11] D. W. DeRoo, "Determination of Young's modulus of polysilicon using resonant micromechanical beams," M.S. Report, Dept. of Electrical and Computer Engineering, University of Wisconsin - Madison, January 1988.
- [12] M. W. Putty, "Polysilicon resonant microstructures," M.S. Thesis, Dept. of Electrical Engineering and Computer Science, The University of Michigan, Ann Arbor, Mich., September 1988.
- [13] M. A. Schmidt, "Microsensors for the measurement of shear forces in turbulent boundary layers," Ph.D. Thesis, Massachusetts Institute of Technology, Cambridge, Mass., May 1988.
- [14] M. A. Schmidt, R. T. Howe, S. D. Senturia, and J. H. Haritonidis, "Design and calibration of a microfabricated floating-element shear-stress sensor," *IEEE Trans. on Electron Devices*, **35**, 750-757, (1988).
- [15] A. P. Pisano, "Resonant-structure micromotors," *Technical Digest*, IEEE Micro Electromechanical Systems Workshop, Salt Lake City, Utah, February 20-22, 1989.
- [16] R. T. Howe, "Integrated silicon electromechanical vapor sensor," Ph.D. Thesis, Dept. of Electrical Engineering and Computer Sciences, University of California at Berkeley, December 1984.
- [17] A. M. Wahl, *Mechanical Springs*, 1<sup>st</sup> edition, (Cleveland: Penton), 1945.
- [18] T. A. Lober and R. T. Howe, "Surface-micromachining processes for electrostatic microactuator fabrication," *Technical Digest*, IEEE Solid-State Sensor and Actuator Workshop, Hilton Head Island, South Carolina, June 6-9, 1988, 59-62.
- [19] H. Guckel, T. Randazzo, and D. W. Burns, "A simple technique for the determination of mechanical strain in thin films with applications to polysilicon," *J. Appl. Phys.*, **57**, 1671-1675, (1985).
- [20] T. A. Lober, J. Huang, M. A. Schmidt, and S. D. Senturia, "Characterization of the mechanisms producing the bending moments in polysilicon micro-cantilever beams by interferometric deflection measurements," IEEE Solid-State Sensor and Actuator Workshop, Hilton Head Island, South Carolina, June 6-9, 1988, 92-95.
- [21] D. W. Burns, "Micromechanics of integrated sensors and the planar processed pressure transducer," Ph.D. Thesis, Dept. of Electrical and Computer Engineering, University of Wisconsin - Madison, May 1988.
- [22] SuperSAP, Algor Interactive Systems, Inc., Essex House, Pittsburgh, Penn. 15206.
- [23] M. W. Putty, S.-C. Chang, R. T. Howe, A. L. Robinson, and K. D. Wise, "Modelling and characterization of one-port polysilicon resonant microstructures," *Technical Digest*, IEEE Micro Electromechanical Systems Workshop, Salt Lake City, Utah, February 20-22, 1989.
- [24] M. V. Andres, K. W. H. Foulds, and M. J. Tudor, "Sensitivity of a frequency-out silicon pressure sensor," *Technical Digest*, Eurosensors, 3<sup>rd</sup> Symposium on Sensors & Actuators, Cambridge, England, September 22-24, 1987, 18-19.